Journal of the Meteorological Society of Japan

EARLY ONLINE RELEASE

The DOI for this manuscript is
DOI:10.2151/jmsj.2022-050
J-STAGE Advance published date: September 6th, 2022
The final manuscript after publication will replace the preliminary version at the above DOI once it is available.

On the Existence of the Predictability Barrier in the Wintertime Stratospheric Polar Vortex: Intercomparison of Two Stratospheric Sudden Warmings in 2009 and 2010 Winters

Hitoshi MUKOUGAWA [1]

Graduate School of Science, Kyoto University, Kyoto, Japan

Shunsuke NOGUCHI

Department of Earth and Planetary Sciences, Kyushu University
Fukuoka, Japan

Yuhji KURODA

Meteorological Research Institute, Tsukuba, Japan

and

Ryo MIZUTA

Meteorological Research Institute, Tsukuba, Japan

Submitted on April 21, 2022
Revised on July 7, 2022

----

1) Corresponding author: Hitoshi Mukougawa, Graduate School of Science, Kyoto University, Kitashirakawa Oiwake-Cho, Sakyo-Ku, Kyoto, 606-8502 JAPAN
Email: mukou@kugi.kyoto-u.ac.jp
Tel: +81-75-753-4273
Fax: +81-75-753-4278

Abstract

To compare the predictability of two stratospheric sudden warming (SSW) events occurring in 2009 and 2010, ensemble forecast experiments are conducted using an Atmospheric General Circulation Model (AGCM). It is found that the predictable period of the vortex splitting SSW in 2009 is about 7 days which is much shorter than that of the vortex-displacement SSW in 2010. The latter event is predictable more than 13 days in advance. The ensemble spread in the upper stratosphere for medium-range forecasts is found to be enlarged just prior to the onset of the 2009 SSW event, while no such enlargement is seen for the 2010 SSW event.

Stability analysis of the zonally asymmetric basic states specified by the ensemble mean forecast using a nondivergent barotropic vorticity equation reveals that the extremely distorted polar vortex in the upper stratosphere just before the onset of the 2009 SSW event is highly unstable to infinitesimal perturbations, whereas there is no such unstable mode with an extremely large growth rate during the 2010 SSW event. In addition, the most unstable mode during the onset of the 2009 SSW event has a similar horizontal structure to the 1st EOF of the ensemble spread. Thus, it is suggested that a predictability barrier inherent in the upper stratospheric circulation, characterized by the presence of dynamically unstable modes with large growth rates limits the predictable period of the 2009 SSW event.

Keywords stratospheric sudden warming; predictability; stability analysis; barotropic vorticity equation

1. Introduction

Stratospheric sudden warming (SSW) events are the most spectacular phenomena in the wintertime stratospheric circulation. Recent observational studies have elucidated that they exert significant impacts on weather and climate in the troposphere through promoting downward migration of the annular mode (Thompson and Wallace 2001; Baldwin and Dunkerton 2001) or causing downward propagation of stratospheric planetary waves (Kodera et al. 2008; Kodera et al. 2016; Mukougawa et al. 2017). Pioneering studies to examine the predictability of SSW events (Mukougawa and Hirooka 2004; Mukougawa et al. 2005) by using operational extended-range forecasts indicated that some SSWs have prolonged predictable periods of more than two weeks. Hence, SSW events have been one of the promising elements leading to higher prediction skills of extended-range forecasts through their downward influence on the troposphere (Butler et al. 2019).

It has been documented that the predictable period of SSW events ranges from 6 to 30 days (Tripathi et al. 2015; Ichimaru et al. 2016; Karpechko 2018). Taguchi (2016) analyzed 1-month hindcast data from 1979 to 2012 provided by the Japan Meteorological Agency (JMA) and indicated a possible connection between the predictability of SSWs and the geometry of polar vortices: vortex splitting SSWs are less predictable than vortex displacement SSWs. Domeisen et al. (2020) also confirmed the dependence of predictability on SSW type based on six displacements and five split SSW events. However, the mechanism producing such dependence of predictability has not been elucidated yet.

Because the SSW is primarily caused by the upward propagation of amplifying planetary waves in the troposphere (Matsuno 1971), the predictability of anomalous tropospheric circulations is an important agent to limit the predictable skill of the stratospheric circulation. Mukougawa et al. (2005) indicated the skillful forecast of tropospheric blocking is a key to reproducing a vortex displacement SSW occurring in 2001 with a prolonged predictable period of at least 2 weeks. On the other hand, Noguchi et al. (2016) (hereafter N16) conducted a series of ensemble hindcast experiments initialized at 1-day interval and indicated that forecasts of a vortex splitting SSW occurring in 2009 with a short predictable period of 6 days have high sensitivity to the initial upper stratospheric circulation. Thus, the dynamics of stratospheric circulation would also play an important role in determining the predictability of the SSW.

The dynamical instability of the upper stratospheric circulation with zonally asymmetric components is likely to contribute to high sensitivity of the forecast to the initial stratospheric state. Mukougawa et al. (2017) (hereafter M17) computed unstable modes using a vorticity equation linearized about the basic state specified by the ensemble mean prediction of an Atmospheric General Circulation Model (AGCM) and found that zonally asymmetric upper stratospheric circulation in early March 2007 when downward propagating planetary waves were observed in the stratosphere is highly unstable to infinitesimal perturbations. They attributed a short predictable period of about 7 days for the downward propagating event to the existence of a predictability barrier in the stratosphere associated with the dynamical instability of large growth rates. Moreover, they hypothesized that the obtained unstable mode in the upper stratosphere acts as a precursor for the emergence of the downward propagating planetary waves in the stratosphere.

In this paper, we will pursue the role of dynamical instability of stratospheric circulation in limiting the predictability of SSW events. If the stratospheric circulation during the onset phase of an SSW event is highly unstable, we can argue for the existence of a predictability barrier in the stratosphere which limits the predictable period of the SSW. For this purpose, first, the same AGCM used in N16 will be utilized to conduct ensemble forecast experiments for the winters of 2009 and 2010 to compare the predictability of the 2009 vortex splitting SSW and the 2010 vortex displacement SSW. As shown by Ayarzagüena et al. (2011) and Figure 1 below, the two SSW events occur on approximately the same calendar day. Hence, the potential influence of differences related to time in the seasonal cycle can be neglected when comparing the predictability of the two SSWs. It is noted, however, that other external factors affecting the wintertime polar stratosphere, such as the phase of the QBO and the sunspot cycle, were dissimilar in both winters as pointed out by Ayarzagüena et al. (2011). Second, as in M17, an eigenvalue analysis will be conducted for both winters using a vorticity equation linearized about the ensemble mean forecast at each pressure level, and the stability property of the distorted polar vortex is compared for both winters. The role of the obtained unstable modes in the time evolution of the SSW event will be also discussed.

2. Data and Model

2.1 Reanalysis data

As in N16, the 6-hourly ERA-Interim reanalysis dataset (Dee et al. 2011) is used for both the analysis and in constructing initial conditions for the ensemble reforecast experiments. The ERA-Interim dataset has 37 vertical pressure levels extending up to 1 hPa at grid intervals of 1.25° longitude and 1.25° latitude. Daily means consisting of four values every six hours from 00UTC to 18UTC are used for the analysis.

2.2 Ensemble forecast data

As in N16, we conduct ensemble forecasts of 25 members starting at 12UTC every day during January 2010 using the ensemble prediction system of the Meteorological Research Institute (MRI-EPS) (Yabu et al. 2014) and MRI-AGCM (Mizuta et al. 2006, 2012) both having a horizontal resolution of TL159 and 60 vertical levels with the top boundary at 0.1 hPa. Each ensemble forecast consisting of 24 perturbed initial conditions created by the MRI-EPS and one unperturbed initial condition specified by the ERA-Interim is performed using MRI-AGCM. There are 25 model levels at pressures less than 100 hPa while 14 levels at pressures less than 10 hPa for MRI-EPS, MRI-AGCM, and ERA-Interim (JMA 2014; Fujiwara et al. 2017). The model settings of MRI-AGCM are all the same as those in N16. We also reexamine ensemble forecasts starting every day during January 2009, which were used in N16. Daily-mean prediction data on 2.5° by 2.5° horizontal grids with 38 vertical pressure levels with a top at 0.4 hPa computed from 6-hourly model outputs are analyzed.

2.3 Non-divergent barotropic vorticity equation on a sphere

To examine the dynamical stability of stratospheric circulations, we utilize the following non-divergent barotropic vorticity equation on a sphere linearized about the specified basic flow denoted by the notation overbar $\bar{(\ )}$ as in M17:

$$\frac{\partial \zeta'}{\partial t} + J(\bar{\psi}, \zeta') + J(\psi', \bar{\zeta}) + \frac{2\Omega}{a^2}\frac{\partial \psi'}{\partial \lambda} = \nu\left(\Delta + \frac{2}{a^2}\right)^3 \zeta'. \tag{1}$$

Here, $\psi(\lambda, \mu, t)$ is the stream function, λ the longitude, μ the sine of the latitude, t the time, $\zeta \equiv \Delta\psi$ the relative vorticity, Ω the angular velocity of the rotation of the earth with the radius a, Δ the horizontal Laplacian, and $J(\alpha, \beta)$ the horizontal Jacobian operator on a sphere. The infinitesimal perturbations are indicated by prime ($'$). A scale-selective hyperviscosity term with a coefficient ν are introduced on the right-hand side of Eq. (1).

Then, normal mode solutions of the perturbation

$$\psi'(\lambda, \mu, t) = \mathrm{Re}\{\phi(\lambda, \mu)e^{\sigma t}\}, \tag{2}$$

where $\sigma = \sigma_r + i\sigma_i$, are obtained by solving a matrix eigenvalue problem after expanding the basic flow and the perturbation $\phi(\lambda, \mu)$ into spherical harmonics. The growth rate and the frequency of the perturbation are given by σ_r and σ_i in Eq. (2), respectively. The spatial resolution of the model used in the computation is T63 (triangular truncation at the total wavenumber N = 63) while the basic flow is triangularly truncated at N = 21 to smooth out small scale structures. An efficient code of ISPACK (Ishioka 2018) for the associated Legendre functions is implemented in the model. The hyperviscosity coefficient ν in Eq. (1) is specified by a small constant giving a dissipation time scale of 0.1 days at N = 85. These model settings are all the same as those in M17.

3. Results

3.1 Predictability of the 2009 and 2010 SSWs

Fig. 1

Figure 1a indicates the time evolution of 10-hPa zonal-mean zonal wind averaged poleward of 60°N during the 2009 and 2010 winters for the analysis (ERA-Interim). In both winters, westerlies prevailing in the first half of January decelerate after 15 January and are replaced by easterlies on 24 January (hereafter referred to as day 0), coincidentally (Ayarzagüena et al. 2011). On day 0 of the 2009 winter, the polar vortex for the analysis is broken into two vortices, characterizing the vortex splitting SSW event (Fig. 1b). On the other hand, the polar vortex for the analysis is displaced off the pole on day 0 of the 2010 winter, corresponding to the vortex displacement SSW event (Fig. 1c).

Fig. 2

The predictability of each SSW event was assessed by the spatial anomaly correlation coefficient (ACC) for 10-hPa geopotential height field poleward of 40°N using a box-and-whisker diagram (Fig. 2) . For the 2009 SSW event (Fig. 2a), the ACC of the ensemble mean forecast on day 0 (24 January) becomes larger than 0.6 for forecasts starting after day −9. However, the spread among ensemble members is considerably large, and ACCs of some members are lower than 0.6 for those forecasts. Since the spread of forecasts starting after day −7 (17 January) becomes small and ACCs of all forecasts are larger than 0.6 on day 0, the predictable period of the 2009 SSW event can be evaluated to be about 7 days. On the other hand, the ACC of the ensemble mean forecast for the 2010 SSW event on day 0 (Fig. 2b) is larger than 0.6 even for the forecast from day −15 (9 January), but the spread is still large with a couple of members having ACCs less than 0.6. The day 0 spreads also become much smaller in the forecasts after day −13 (11 January). Hence, the predictable period of the 2010 SSW event can be evaluated to be about 13 days. Note that the day 0 spreads in the forecasts from day −7 and −5 for the 2010 SSW event are smaller than those for the 2009 SSW event.

The enhanced spread for the 2009 SSW compared with the 2010 SSW can be recognized in Fig. 3, which shows contours at 5-hPa geopotential height of 34500 m on 21 January 2009 (day −3) and 33600 m on 20 January 2010 (day −4) for the analysis (red lines) and the 4-day forecast (black lines). For the 2009 SSW (Fig. 3a), some members predict the complete splitting of the polar vortex, whereas others predict the still connected state (which recovers to the single vortex state immediately after that as shown in N16), corresponding to a large spread. For the 2010 SSW, all ensemble members successfully predict the shape of the polar vortex and its displacement from the North Pole. As a result, the spread is very small as shown in Fig. 2.

Fig. 3

An upsurge in the growth of the ensemble spread of the upper stratospheric geopotential height field just prior to the onset of the 2009 SSW (day 0) is also recognized in Fig. 4a. This figure shows the time evolution of the rms ensemble spread during the 10-day forecast

Fig. 4

based on the 5-hPa geopotential height field north of 30°N. The rms ensemble spread at a lead time *i* was defined by $\sqrt{\frac{1}{M}\sum_{j=1}^{M}\langle x_j^i - \overline{x^i}\rangle}$, where x_i^j is the predicted 5-hPa geopotential height at a lead time *i* for an ensemble member *j*, *M* is the total number of members in the ensemble forecast, $\overline{x^i}$ is the ensemble mean forecast at a lead time *i* (the average of x_i^j over *M*), and ⟨ ⟩ means the area average north of 30°N. The upsurge is distinct for forecasts with a forecast period of 4 days (red circles) or longer. In particular, the 7-day forecast spread (blue circles) just before day 0 becomes more than twice as large as in early January. On the other hand, this increase in upper stratospheric forecast spread is not seen during the onset of the 2010 SSW but rather becomes larger after day 0 (Fig. 4b).

The enhanced amplification of the spread just prior to the onset of the 2009 SSW is Fig. 5
limited to the upper stratosphere, as shown in Fig. 5a. This figure shows the amplification rate of the rms spread of the geopotential height field north of 30°N at each pressure level during the first 4-day forecast. The amplification rate at each pressure level was evaluated using the ratio of the 4-day forecast spread to the spread at the initial time for each ensemble forecast. Note that the 4-day spread alone cannot accurately determine the amplification rate because the spread at the initial time is a finite value and fluctuates daily as shown in Fig. 4. It can be recognized from Fig. 5a that the 5-hPa amplification rate reaches a maximum of about 15 on days −3 and −2. In the middle and lower stratosphere, such an increase in spread amplification rate is rarely seen. Hence, it is suggested that there is a predictability barrier in the upper stratosphere just prior to the onset of the 2009 SSW, limiting

the predictable period of the upper stratospheric circulation. On the other hand, such an increase in the spread amplification rate is not present just prior to the onset of the 2010 SSW throughout the stratosphere (Fig. 5b). Rather, the amplification rate tends to decrease just before day 0. Thus, the upper-stratospheric predictability barrier did not exist for the 2010 SSW, and the forecast skill of the occurrence of the 2010 SSW was much higher than that of the 2009 SSW.

Fig. 6

The horizontal pattern with the greatest spread among ensemble members can be inferred by EOF analysis of the difference field of each ensemble member from the ensemble mean forecast (Fig. 6). The EOF for each verification day was determined based on the 5-hPa geopotential height north of 30°N using the 4-day ensemble forecast. Magnitudes of the anomalies in Fig. 6 are those attained when the corresponding principal components (PCs) are equal to one standard deviation (Kimoto and Ghil, 1993). The 1st EOFs during the onset of the 2009 SSW were dominated by a wavenumber 2 pattern at high latitudes, which effectively affected the shape of the elongated polar vortex, causing it to split or merge (upper panels in Fig. 6). For the 2010 SSW, the 1st EOFs from the same period from day −6 to day −3 were characterized by a center of action with a somewhat confined structure over North America at high latitudes (lower panels in Fig. 6). In addition, these amplitudes were smaller than the corresponding EOFs for the 2009 SSW. Hence, the shape of the displaced vortex for each ensemble member will be nearly identical, as shown in Fig. 3b.

3.2 Stability analysis using barotropic model

In the above analyses using the ensemble forecasts during the onset period of the 2009 and 2010 SSWs, it has been revealed that the predictability barrier characterized by the rapid spread growth in the upper stratosphere was present for the 2009 SSW while it was absent for the 2010 SSW. Such a predictability barrier would relate to the dynamical instability of the ensemble mean field with zonally asymmetric components as shown in M17. Hence, following M17, we conducted an eigenvalue analysis of the ensemble mean field at each pressure level based on the linearized non-divergent barotropic vorticity equation on a sphere given by Eq. (1).

Figure 7 shows the growth rate of the most unstable mode computed for the basic flow given by the predicted 5-hPa stream function of the ensemble mean forecast as a function of the initial date of the forecast (the ordinate) and the verification date (the abscissa). This figure clearly shows the existence of the predictability barrier characterized by unstable modes with huge growth rates on days −4 and −3 for the 2009 SSW (Fig. 7a). The barrier exists independent of the forecast period if it is less than 8 days. The growth rate calculated based on the 4-day forecast (the slanting blue line) has a maximum value greater than 1.0 day^{-1} on day −4. It is noteworthy that as the forecast period increases beyond 7 days, the growth rate generally declines with the increase of the forecast period (M17). This is because the ensemble mean forecast tends to converge to the climatology (Murphy 1988) and lose characteristic flow configurations related to SSW as the forecast period increases.

Fig. 7

Meanwhile, when the forecast period is shorter than 2 days, the dependence of the growth rate on the characteristic flow configuration is well recognized (Fig. 7a), but the corresponding time variability of the spread is smaller (Fig. 4a) because the period over which the perturbation grows is also shorter. Hence, it is difficult to discuss the relationship between the spread and the dynamical stability in such short forecast periods. Then, we decided to examine the relationship using 4-day forecasts which clearly preserve the distinct time variation in spreads and growth rates associated with the occurrence of the SSW in 2009 in the following. On the other hand, for the 2010 SSW, growth rates of the most unstable mode obtained from the eigenvalue problem using the 4-day ensemble mean forecast as the basic state are relatively small, less than 0.5 even on days −4 and −3 (Fig. 7b). There is also no clear increase in the growth rate just before day 0, indicating that there is no enhanced predictability barrier in the upper stratosphere prior to the onset of the 2010 SSW.

Figure 8 shows the height-time cross-section of the growth rate of the most unstable mode, computed using the 4-day ensemble mean forecast as the basic state in Eq. (1). For the 2009 SSW, the predictability barrier characterized by a large growth rate is confirmed in the upper stratosphere from 5 hPa to 1 hPa on day −4. The maximum amplification rate of the 5-hPa spread during this period is about 15 (Fig. 5a), corresponding to a growth rate of 0.68 day^{-1}. This is roughly comparable to the average growth rate of the unstable mode (Fig. 8a). Thus, the spread growth can be explained by the amplification of initial perturbations

Fig. 8

due to the energetic unstable modes in the upper stratosphere. In contrast, there is no upper stratospheric barrier for the 2010 SSW. Thus, the contrasting predictability characteristics of the two SSWs shown in Fig. 5 are also confirmed by the stability analysis on the ensemble mean field. In the middle and lower stratosphere, growth rates are relatively small for both SSW events. On the other hand, growth rates in the upper troposphere have moderate values and may show peaks, corresponding to the onset of blockings (not shown).

The horizontal structure of the two most unstable modes during the onset period of the 2009 SSW is shown in Fig. 9, along with the 5-hPa stream function of the 4-day ensemble mean forecast specified as the basic state (upper panel). During this period, the basic state is characterized by a gradually elongating polar vortex and eventual vortex splitting, with a predominant wavenumber 2 structure at high latitudes. In this period, energetic unstable modes with wavenumber 2 structure localized within the elongated polar vortex of the basic state are found to exist: they are the first mode on day −6, the second mode on day −5, the first mode on day −4, and the second mode on day −3. It should be noticed that the unstable modes in the period from day −7 to day −4 have a similar horizontal structure to the 1st EOF (Fig. 6d) of the 4-day forecast starting from day −7. As discussed in Appendix, the resemblance indicates that these unstable modes play an important role in the formation of the predictability barrier during the onset period of the 2009 SSW. It is also interesting to note that the phase of the most unstable mode (the middle panel of Fig. 9c) is shifted by almost a quarter wavelength from that of the basic flow (the top panel of Fig. 9c). When the

Fig. 9

perturbation satisfies such a phase relationship with the basic flow, the kinetic energy growth of the perturbation becomes maximum as shown by Hirota (1967) from an argument based on the kinetic energy conversion from the basic flow to the perturbation.

The role of the unstable mode in the ensemble prediction of the 2009 SSW can be well Fig. 10 recognized from Fig. 10, which shows the time evolution of the horizontal structure of the most unstable mode on day −4 (middle panel of Fig. 9c) for each quarter of the cycle. Since the basic state specified for the eigenvalue problem has zonally asymmetric components, the structure of the obtained mode varies considerably depending on its phase as shown in Simmons et al. (1983). The bottom panels show the superposition of the basic state and the most unstable mode at each phase shown in the upper panels. The amplitude of the mode was specified so that the square root of the variance of the stream function at the initial phase (Phase 0 in Fig. 10a) is 7.24% of that of the basic state. The ratio is based on the rms ensemble spread of the 4-day forecast of 5-hPa geopotential height (72.78 m, Fig. 4a) and the square root of the variance of the 5-hPa geopotential height north of 30°N on 20 January for the analysis (1005 m). The composited fields show polar vortex splitting (Figs. 10c and 10d) and merging (Figs. 10a and 10b) depending on the phase of the unstable mode, which well resembles the characteristic variability of the polar vortices predicted during the onset of the 2009 SSW event shown in Fig. 3a. The relationship between the variability of the horizontal structure of the unstable mode depending on its phase and that of the predicted polar vortices among ensemble members is also discussed in Appendix. This fact also confirms the primarily important role of the unstable modes residing in the upper stratosphere in the ensemble prediction of the 2009 SSW. On the other hand, unstable modes in the upper stratosphere during the onset of the 2010 SSW are considered to play only a secondary role in the ensemble forecast, since they have a relatively smaller horizontal structure embedded in the distorted polar vortex of the basic state (not shown) and a small growth rate (Fig. 8b).

4. Concluding Remarks

To compare the predictability of two stratospheric sudden warming (SSW) events occurring in 2009 and 2010, ensemble reforecast experiments were conducted using the ensemble prediction system of the Meteorological Research Institute (MRI-EPS) and MRI-AGCM. It was found that the predictable period of the vortex-splitting SSW in 2009 was about 7 days, much shorter than that of the vortex-displacement SSW in 2010, which was predictable more than 13 days in advance. The ensemble spread of the geopotential height in the upper stratosphere for medium-range forecasts was found to be enlarged just prior to the onset of the 2009 SSW, while no such enlargement was seen for the 2010 SSW. Hence, it is suggested that the predictability barrier inherent to the upper stratospheric circulation limits the predictable period of the 2009 SSW.

We then investigated the dynamical basis for such predictability barrier in the upper stratosphere by performing a stability analysis of the stratospheric circulation using the non-divergent barotropic vorticity equation as in M17. As a result, it was revealed that the upper stratospheric circulation with zonally asymmetric components specified by the ensemble mean forecast was highly unstable to infinitesimal perturbations during the onset of the 2009 SSW but did not show such enhanced instability during the 2010 SSW. The contrasting stability property during the onset of the two SSWs was similar to the contrasting behavior of the spread growth observed during the same periods. The most unstable mode during the onset of the 2009 SSW had a similar horizontal structure to the ensemble spread as well as the 1^{st} EOF and represents the predicted polar vortex variability as the nearly split polar vortex further elongates or contracts. Therefore, the predictability barrier inherent to the upper stratospheric circulation during the onset of the 2009 SSW can be attributed dynamically to the presence of enhanced instability associated with the highly distorted polar vortex. In addition to the tropospheric predictability barrier associated with the maintenance of tropospheric blocking sustaining the upward propagation of planetary waves as shown in Mukougawa et al. (2005), this study reveals the presence of the upper stratospheric predictability barrier limiting the predictable period of SSW.

The dynamical link between this unstable mode with extremely large growth rates and the prediction of the 2009 SSW can also be confirmed by the results of Coy and Reynolds (2014). They used a dry mechanistic multilayer model to compute stratospheric singular vectors (SVs) during the onset of the 2009 SSW. The first SV (SV1) for an optimization time of 3 days, initialized on 22 January 2009, shown in Fig. 5b of their paper, has a horizontal structure very similar to the most unstable mode obtained in our study (Fig. 9c). In addition, the SV1 has a large amplitude in the upper stratosphere and shows an amplification rate[1] of about 1.1 day^{-1} which is comparable to the maximum growth rate of the unstable mode at 5 hPa (Fig. 8a). These similarities between the most unstable mode and the SV1 also support that the most unstable mode played an important role in the predictability of the 2009 SSW.

The unstable modes for the 2009 SSW in the basic flow dominated by the wavenumber 2 component have much larger growth rates than those for the 2010 SSW dominated by the wavenumber 1 component as shown in Fig. 8. This instability characteristic is consistent with the results of Hirota (1967). In addition, the growth rate of the unstable modes for the 2009 SSW is much larger than that of unstable modes reported by Manney et al. (1991) and Frederiksen (1982): The former paper indicated that the growth rate of the unstable mode for the observed 5-hPa circulation in the Southern Hemisphere during 8-12 September 1982, characterized by amplified wavenumber 2 planetary waves, was at most 0.50 day^{-1}. The latter reported that the growth rate of the unstable mode for the stratospheric circulation with a moderately amplified wavenumber 1 component corresponding to 12 days before the onset of the simulated SSW was 0.14 day^{-1}.

The enhanced growth rate of the 5-hPa unstable mode on day −4 for the 2009 SSW

[1] This is roughly estimated from the maximum value of the initial and final SV1 structures shown in Figs. 5a and 5b of their paper.

could be dynamically attributed to the extremely amplified wavenumber 2 component in the basic flow. In fact, the amplitude of the observed wavenumber 2 component of the 5-hPa geopotential height at 60°N was maximal on day −5 and the elongation of the polar vortex was most pronounced on day −4 as seen in Fig. 9c. Hirota (1967) and Manney et al. (1991) documented that the growth rate of unstable modes increases as the prescribed amplitude of the wavenumber 2 component of the basic flow increases. Hence, the temporal behavior of the growth rate during the onset of the 2009 SSW is roughly consistent with their results. However, the dependence of the growth rate on the amplitude of the wavenumber 2 component has not yet been clarified dynamically. Hence, the next study should take the same approach as Hirota (1967), using a basic flow with an idealized horizontal structure to reveal the dynamical basis of the barotropic instability of the elongated polar vortex.

Finally, it should be noted that the unstable modes with large growth rates exist for the splitting polar vortex in the upper stratosphere (Figs. 7 and 8), whose forecast data is not widely provided in the current frameworks (e.g., hindcast datasets archived in the subseasonal-to-seasonal prediction project of the World Weather Research Programme (WWRP) and the World Climate Research Programme (WCRP) only include variables up to the 10-hPa pressure level). Therefore, previous studies for the predictability of SSWs using such low-top datasets would not realize the predictability barrier in the upper stratosphere highlighted in this study. Hence, we would like to emphasize the importance of analyzing the upper stratospheric circulation in order to clarify the dependence of SSW predictability on the shape of the polar vortex. It is also hoped that more upper stratospheric datasets will be archived and provided by many operational/modeling centers to further investigate the role of unstable modes in the evolution of SSW. When analyzing climate model simulations to infer the causes of poorly represented stratospheric polar vortex variability (e.g., Hall et al. 2021), attention should be paid to the upper stratospheric circulation.

Data Availability Statement

The ERA-Interim data is available from the ECMWF website: (https://www.ecmwf.int/en/forecasts/datasets/reanalysis-datasets/era-interim). The dataset of the ensemble forecast analyzed in this study is available from the corresponding author on reasonable request.

Acknowledgments

A spectral transformation library ISPACK (http://www.gfd-dennou.org/arch/ispack/) developed by Prof. K. Ishioka was used to solve the eigenvalue problem for the non-divergent barotropic vorticity equation. The authors would like to thank his kind instruction on how to use ISPACK library. Thanks are also extended to Prof. Masatomo Fujiwara and two anonymous reviewers for their thoughtful comments and critical reading. H.M. would like to express his sincere thanks to Prof. I. Hirota who has given him continuing guidance and encouragement throughout this work. Figures were drawn using GFD-DENNOU Library. This study was partly supported by Grants-in-Aid for Scientific Research 18H01280 funded by Japan Society of the Promotion of Science.

Appendix

Unstable mode, Spread, and 1st EOF

Fig. A1

We discuss the relationship between the most unstable mode, ensemble spread, and 1st EOF during the onset period of the 2009 SSW. Let's consider the time evolution of the trajectory associated with each ensemble member during a period from the initial time t_i to the verification time t_v in phase space. We assume that the most unstable mode for the basic state specified by the predicted ensemble mean forecast is the same during the period, of which assumption is approximately valid from day −7 (t_i) to day −4 (t_v) as confirmed in Fig. 9. If the time evolution is exclusively determined by the most unstable mode in the framework of the linear dynamics and initial perturbations of ensemble forecasts are randomly chosen with the same projected magnitude onto the eigenfunction $\phi(\lambda,\mu)$ of the most unstable mode (Eq. (2); Mukougawa 1988), then the square root of the variance associated with the ensemble spread of the stream function at t=t_i would be

$$g(\lambda,\mu) = \sqrt{\frac{1}{2\pi}\int_0^{2\pi} \mathrm{Re}\{\phi(\lambda,\mu)\exp(i\alpha)\}^2\, d\alpha}. \qquad \text{(A1)}$$

Here, α is the phase of the most unstable mode. Note that the square root of the variance at t is also given by $g(\lambda,\mu)$ if we ignore the temporal amplification with $\exp\{(t-t_i)\alpha_r\}$, where α_r is the growth rate. This is because α will only increase by a certain constant

$(t - t_i)\alpha_i$, where α_i is the imaginary part of the eigenvalue, but the integral range for α is independent of *t* in Eq. (A1).

Now, Fig. A1a shows the horizontal distribution of $g(\lambda, \mu)$ for the most unstable mode on day −4 (Fig. 9c). The magnitude of $g(\lambda, \mu)$ attains its peak at four longitudes along 60°N: around 80°E; 120°E; 120°W; 40°W. On the other hand, Fig. A1b indicates the square root of the ensemble spread of the predicted stream function on day −4, computed using the 4-day ensemble forecast starting from day −7. These two patterns are very similar to each other in the sense that there are four local maxima along 60°N at approximately the same longitude. Of course, as shown in Fig. A1c, the square root of the variance associated with the 1st EOF, which has the largest percentage of variance (57.9%; Fig. 6c), well resembles the latter. Thus, we can confirm the resemblance of the variance associated with the most unstable mode, spread, and the 1st EOF, strongly supporting the validity of the assumption that linear dynamics specified only by the most unstable mode with a large growth rate (Fig. 9c) dominate the time evolution of each ensemble member during the onset period of the 2009 SSW. Hence, it can be recognized that the variability of the horizontal structure of the unstable mode depending on its phase shown in Fig. 10 is closely related to the predicted variability of the polar vortex among the ensemble members (Fig. 3a).

References

Ayarzagüena, B., U. Langematz, and E. Serrano, 2011: Tropospheric forcing of the stratosphere: A comparative study of the two different major stratospheric warmings in 2009 and 2010. *J. Geophys. Res.*, **116**, D18114, doi: 10.1029/2010JD015023.

Baldwin, M. P., and T. J. Dunkerton, 2001: Stratospheric harbingers of anomalous weather regimes. *Science*, **294**, 581-584.

Butler, A. H., A. Charlton-Perez, D. I. V. Domeisen, I. R. Simpson, and J. Sjoberg, 2019: Predictability of Northern Hemisphere final stratospheric warmings and their surface impacts. *Geophys. Res. Lett.*, **46,** 10,578-10,588, doi: 10.1029/2019GL083346.

Coy, L., and C. A. Reynolds, 2014: Singular vectors and their nonlinear evolution during the January 2009 stratospheric sudden warming. *Q. J. R. Meteorol. Soc.*, **140**, 1013-1024, doi: 10.1002/qj.2181.

Dee, D. P., and 35 Coauthors, 2011: The ERA-Interim reanalysis: Configuration and performance of the data assimilation system. *Q. J. R. Meteorol. Soc.*, **137**, 553-597.

Domeisen, D. I. V., and 19 Coauthors, 2020: The role of the stratosphere in subseasonal to seasonal prediction: 1. Predictability of the stratosphere. *J. Geophys. Res. Atmos.,* **125**, e2019JD030920, doi: 10.1029/2019JD030920.

Frederiksen, J. S., 1982: Instability of the three-dimensional distorted stratospheric polar vortex at the onset of the sudden warming. *J. Atmos. Sci.*, **39**, 2313-2329.

Fujiwara, M., and 36 Coauthors, 2017: Introduction to the SPARC Reanalysis Intercomparison Project (S-RIP) and overview of the reanalysis systems. *Atmos. Chem. Phys.*, **17**, 1417-1452, doi: 10.5194/acp-17-1417-2017.

Hirota, I., 1967: Dynamic instability of the stratospheric polar vortex. *J. Meteor. Soc. Japan*, **45**, 409-421.

Hall, R. J., D. M. Mitchell, W. J. Seviour, and C. J. Wright, 2021: Persistent model biases in the CMIP6 representation of stratospheric polar vortex variability. *J. Geophys. Res. Atmos.*, **126**, e2021JD034759, doi: 10.1029/2021JD034759.

Ichimaru, T., S. Noguchi, T. Hirooka, and H. Mukougawa, 2016: Predictability changes of stratospheric circulations in Northern Hemisphere winter. *J. Meteor. Soc. Japan*, **94**, 7-24, doi: 10.2151/jmsj.2016-001.

Ishioka, K., 2018: A new recurrence formula for efficient computation of spherical harmonic transform. *J. Meteor. Soc. Japan*, **96**, 241-249, doi: 10.2151/jmsj.2018-019.

Japan Meteorological Agency, 2014: JRA-55 Product Users' Handbook: Model Grid Data. JMA, Japan, 31 pp. [Available at https://jra.kishou.go.jp/JRA-55/document/JRA-55_handbook_TL319_en.pdf.]

Karpechko, A. Y., 2018: Predictability of sudden stratospheric warmings in the ECMWF extended-range forecast system. *Mon. Wea. Rev.*, **146**, 1063-1075, doi: 10.1175/MWR-D-17-0317.1.

Kimoto, M., and M. Ghil, 1993: Multiple flow regimes in the northern hemisphere winter. Part I: Methodology and hemispheric regimes. *J. Atmos. Sci.*, **50**, 2625-2643.

Kodera, K., H. Mukougawa, and S. Itoh, 2008: Tropospheric impact of reflected planetary waves from the stratosphere. *Geophys. Res. Lett.*, **35**, L16806, doi:

10.1029/2008GL034575.

Kodera, K., H. Mukougawa, P. Maury, M. Ueda, and C. Claud, 2016: Absorbing and reflecting sudden stratospheric warming events and their relationship with tropospheric circulation. *J. Geophys. Res. Atmos.*, **121**, 80-94, doi: 10.1002/2015JD023359.

Manney, G. L., C. R. Mechoso, L. S. Elson, and J. D. Farrara, 1991: Planetary-scale waves in the Southern Hemisphere winter and early spring stratosphere: Stability analysis. *J. Atmos. Sci.*, **48**, 2509-2523.

Matsuno, T., 1971: A dynamical model of the stratospheric sudden warming. *J. Atmos. Sci.*, **28**, 1479-1494.

Mizuta R., and 9 Coauthors, 2006: 20-km-mesh global climate simulation using JMA-GSM model −Mean climate states−. *J. Meteor. Soc. Japan*, **84**, 165-185, doi: 10.2151/jmsj.84.165.

Mizuta R., and 11 Coauthors, 2012: Climate simulations using MRI-AGCM3.2 with 20-km grid. *J. Meteor. Soc. Japan*, **90A**, 233-258, doi: 10.2151/jmsj.2012-A12.

Mukougawa, H., 1988: A dynamical model of “Quasi-stationary” states in large-scale atmospheric motions. *J. Atmos. Sci.*, **45**, 2868-2888.

Mukougawa, H., and T. Hirooka, 2004: Predictability of stratospheric sudden warming: A case study for 1988/99 winter. *Mon. Wea. Rev.*, **132**, 1764-1776.

Mukougawa, H., H. Sakai, and T. Hirooka, 2005: High sensitivity to the initial condition for the prediction of stratospheric sudden warming. *Geophys. Res. Lett.*, **32,** L17806, doi:

10.1029/2005GL022909.

Mukougawa, H., S. Noguchi, Y. Kuroda, R. Mizuta, and K. Kodera, 2017: Dynamics and predictability of downward-propagating stratospheric planetary waves observed in March 2007. *J. Atmos. Sci.*, **74**, 3533-3550, doi: 10.1175/JAS-D-16-0330.1

Murphy, J. M., 1988: The impact of ensemble forecasts on predictability. *Q. J. R. Meteorol. Soc.*, **114**, 463-493.

Noguchi, S., H. Mukougawa, Y. Kuroda, R. Mizuta, S. Yabu, and H. Yoshimura, 2016: Predictability of the stratospheric polar vortex breakdown: An ensemble reforecastmeterization experiment for the splitting event in January 2009. *J. Geophys. Res. Atmos.*, **121**, 3388-3404, doi: 10.1002/2015JD024581.

Simmons, A. J., J. M. Wallace, and G. W. Branstator, 1983: Barotropic wave propagation and instability, and atmospheric teleconnection patterns. *J. Atmos. Sci.*, **40**, 1363-1392.

Taguchi, M., 2016: Connection of predictability of major stratospheric sudden warmings to polar vortex geometry. *Atmos. Sci. Let.*, **17**, 33-38, doi: 10.1002/asl.595.

Thompson, D. W. J., and J. M. Wallace, 2001: Regional climate impacts of the Northern Hemisphere annular mode. *Science*, **293**, 85-89.

Tripathi, O. P., and 15 Coauthors, 2015: The predictability of the extratropical stratosphere on monthly time-scales and its impact on the skill of tropospheric forecasts. *Q. J. R. Meteor. Soc.*, **141**, 987-1003.

Yabu, S., R. Mizuta, H. Yoshimura, Y. Kuroda, and H. Mukougawa, 2014: Meteorological

Research Institute Ensemble Prediction System (MRI-EPS) for climate research. *Tech. Rep. Meteor. Res. Inst.*, **71**, 63 pp.

List of Figures

Fig. 1 (a) Time evolution of the zonal-mean zonal wind averaged poleward of 60°N at 10 hPa (m s^{-1}) during the winter seasons of 2009 (red line) and 2010 (blue line) for the analysis (ERA-Interim). (b) Horizontal distribution of 10-hPa geopotential height (m) on 24 January 2009 for the analysis. Contour interval is 200 m. (c) As in (b), except for 24 January 2010.

Fig. 2 Spatial anomaly correlation coefficient (ACC) for the predicted 10-hPa geopotential height on day 0 (24 January) for ensemble forecasts starting from 9 (day −15) to 19 (day −5) January (the ordinate). The spatial ACC is evaluated poleward of 40°N. The whiskers indicate the full range of ACCs for 25 ensemble members, and the boxes show the range between the 6th value from the largest (24%) and the 7th value from the smallest (76%) ACCs. Short horizontal red lines indicate ACCs for the ensemble mean forecasts.

Fig. 3 Limited contour analysis of polar vortex, showing contours at a prescribed 5-hPa height of 34500 m on 21 January 2009 (a) and 33600 m on 20 January 2010 (b). Thick red curves show the analysis (ERA-Interim). The corresponding 4-day ensemble forecasts are shown by thin black curves.

Fig. 4 Time evolution of the rms ensemble spread (m) during the 10-day forecast based on the 5-hPa geopotential height field north of 30°N. See text for the detailed definition of the rms ensemble spread. (a) January 2009, (b) January 2010. Green, red, and blue solid circles indicate 2-day, 4-day, and 7-day forecasts, respectively.

Fig. 5 (a) Amplification rate of the rms ensemble spread during the 4-day forecast at each pressure level (the ordinate) for each verification date (the abscissa) in January 2009. Spreads were evaluated based on geopotential height fields north of 30°N. Regions with an amplification rate larger than 12.0 are shaded red. The red vertical line denotes day 0 (24 January), and the blue horizontal line represents 5 hPa. (b) As in (a), except for January 2010.

Fig. 6 The 1st EOFs of the difference field of each ensemble member from the ensemble mean prediction of the 5-hPa geopotential height north of 30°N (m) during the onset of the 2009 SSW (top panels) and 2010 SSW (bottom panels) on day −6 (a, e), day −5 (b, f), day −4 (c, g), and day −3 (d, h), computed using 4-day forecasts. Contours are scaled to represent anomalies in meters when the PC is equal to one standard deviation; contour interval is 20 m. Percentage variances associated with the 1st EOFs are shown in the upper right of each panel.

Fig. 7 (a) Growth rate (day^{-1}) of the most unstable mode computed for the basic flow consisting of the T21 truncated 5-hPa stream function of the ensemble mean field on each prediction date (the abscissa) of the forecast starting from 6 to 28 January (the ordinate). The radius of the filled circle is proportional to the growth rate, and its color also indicates the range of the growth rate as shown in the legend. The red vertical line represents day 0 (24 January), and the blue slanting line indicates 4-day forecasts. (b) As in (a), except for January 2010.

Fig. 8 As in Fig. 5, except for the growth rate (day^{-1}) of the most unstable mode computed for the basic flow consisting of the T21 truncated stream function at each pressure level (the ordinate) of the 4-day ensemble mean forecast. Contour interval is 0.1 day^{-1}, and regions where the growth rate is larger than 0.6 (1.0) day^{-1} are lightly (heavily) shaded in red. (b) As in (a), except for January 2010.

Fig. 9 (top) Horizontal structure of the basic flow given by the T21 truncated 5-hPa stream function field (10^7 m^2 s^{-1}) of the ensemble mean prediction on day −6 (a), day −5 (b), day −4 (c), and day −3 (d) for the 4-day forecasts during January 2009. (middle and bottom) Stream function fields for the first and second unstable modes computed for the basic flow. The first and second numbers in parentheses at the top of each panel indicate the growth rate (day^{-1}) and the period (day) of the unstable mode, respectively. Stationary modes with zero imaginary component of eigenvalues are designated by the period of infinity (∞).

Fig. 10 (top) The stream function field of the most unstable mode (middle panel of Fig. 9c) on day −4 at each 1/4 phase of period 2π: (a) phase 0 (initial), (b) phase $\pi/2$, (c) phase π, (d) phase $3\pi/2$. (bottom) As in top panels, except for the composited stream function field (10^7 m^2 s^{-1}) of the basic flow (top panel of Fig. 9c) and the most unstable mode at each 1/4 phase with amplitude α. The amplitude α is specified so that the square root of the variance of the stream function of the unstable mode at the initial phase (a) is 7.24% of that of the basic flow. The variance is evaluated in the region north of 30°N.

Fig. A1 (a) Horizontal distribution for the square root of the variance of the stream function associated with the phase variation of the most unstable mode on day −4 (middle panel of Fig. 9c). (b) As in (a), except for the square root of ensemble spread of the predicted stream function on day −4, computed using the 4-day ensemble forecast starting from day −7. (c) As in (b), except for the absolute value of the regressed stream function anomaly onto PC1 of the ensemble spread on day −4. PC1 is the corresponding principal component score to the 1st EOF shown in Fig. 6c. Contour interval is 2×10^6

$m^2 s^{-1}$ in (b) and (c). The magnitude in (a) is arbitrary.

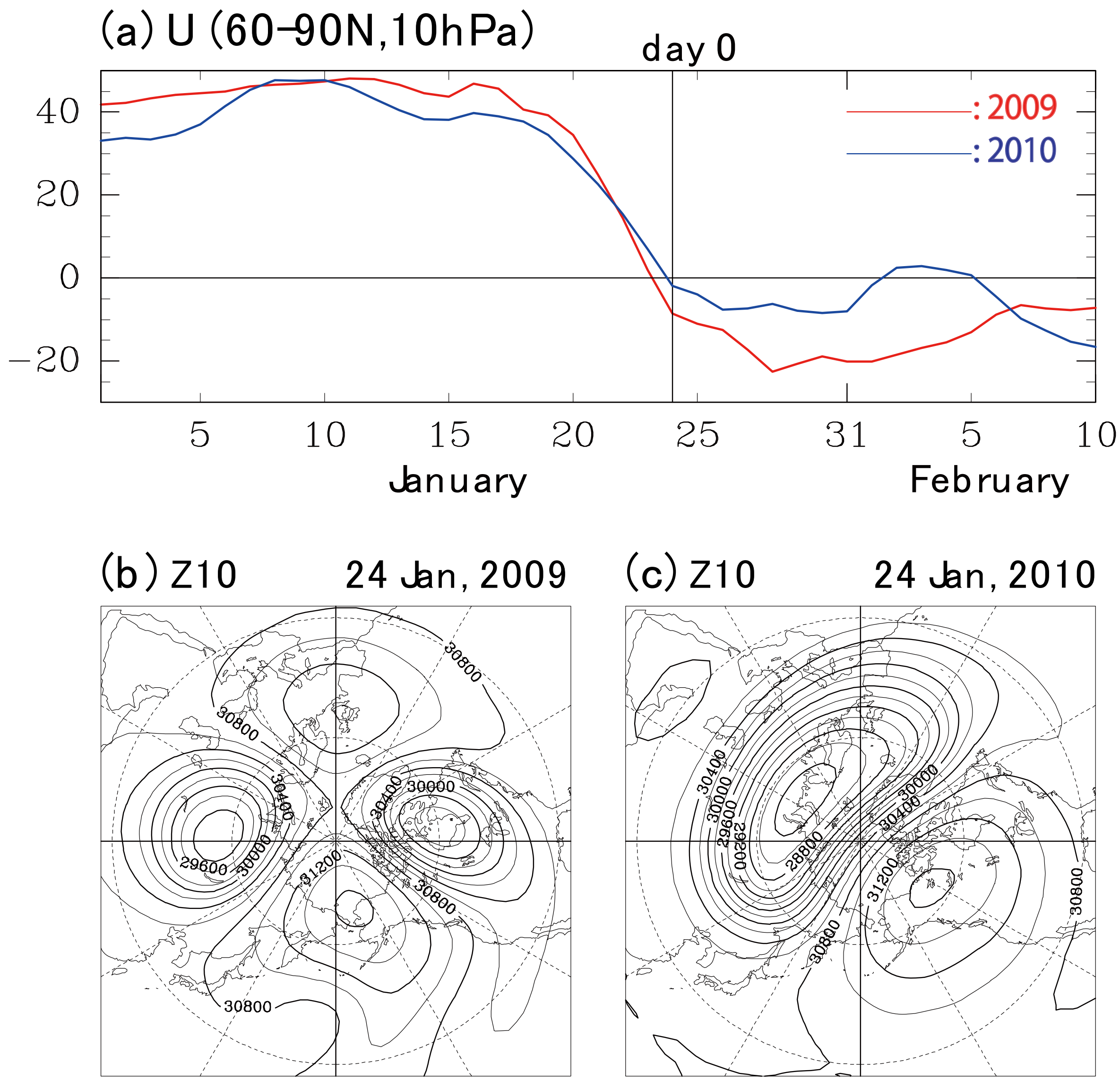

Fig. 1 (a) Time evolution of the zonal-mean zonal wind averaged poleward of 60°N at 10 hPa (m s^{-1}) during the winter seasons of 2009 (red line) and 2010 (blue line) for the analysis (ERA-Interim). (b) Horizontal distribution of 10-hPa geopotential height (m) on 24 January 2009 for the analysis. Contour interval is 200 m. (c) As in (b), except for 24 January 2010.

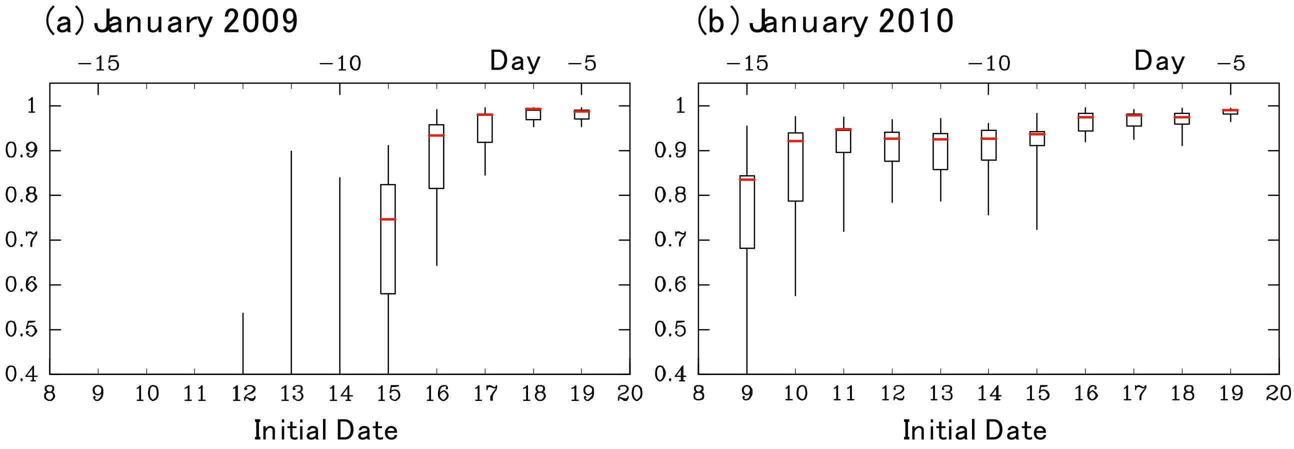

Fig. 2 Spatial anomaly correlation coefficient (ACC) for the predicted 10-hPa geopotential height on day 0 (24 January) for ensemble forecasts starting from 9 (day −15) to 19 (day −5) January (the ordinate). The spatial ACC is evaluated poleward of 40°N. The whiskers indicate the full range of ACCs for 25 ensemble members, and the boxes show the range between the 6th value from the largest (24%) and the 7th value from the smallest (76%) ACCs. Short horizontal red lines indicate ACCs for the ensemble mean forecasts.

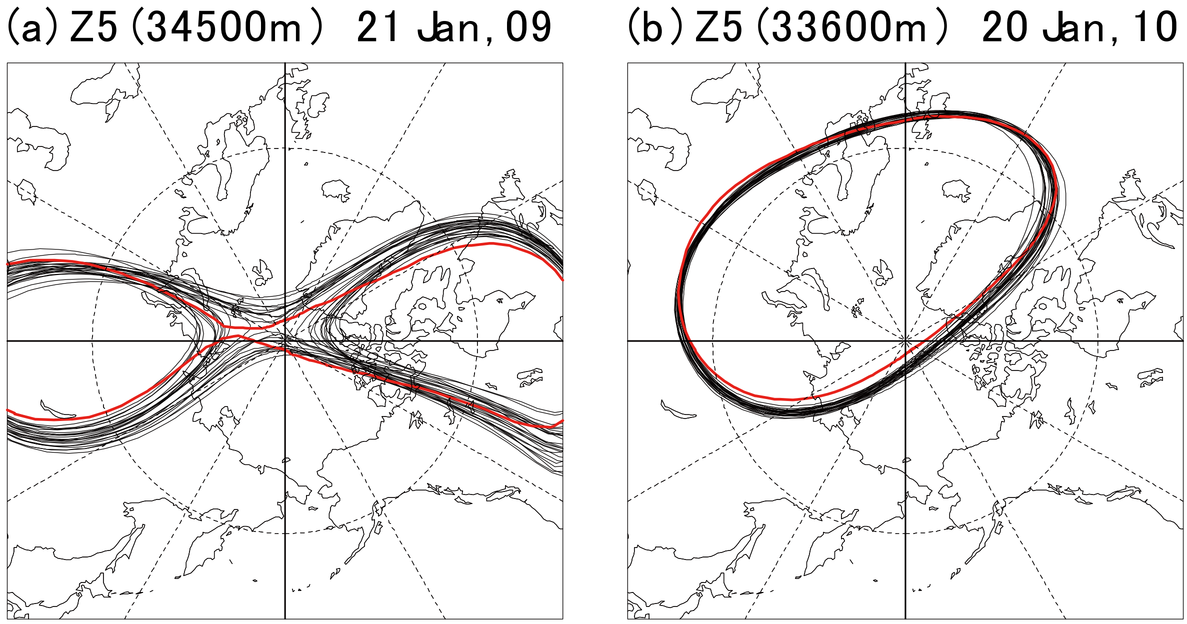

Fig. 3 Limited contour analysis of polar vortex, showing contours at a prescribed 5-hPa height of 34500 m on 21 January 2009 (a) and 33600 m on 20 January 2010 (b). Thick red curves show the analysis (ERA-Interim). The corresponding 4-day ensemble forecasts are shown by thin black curves.

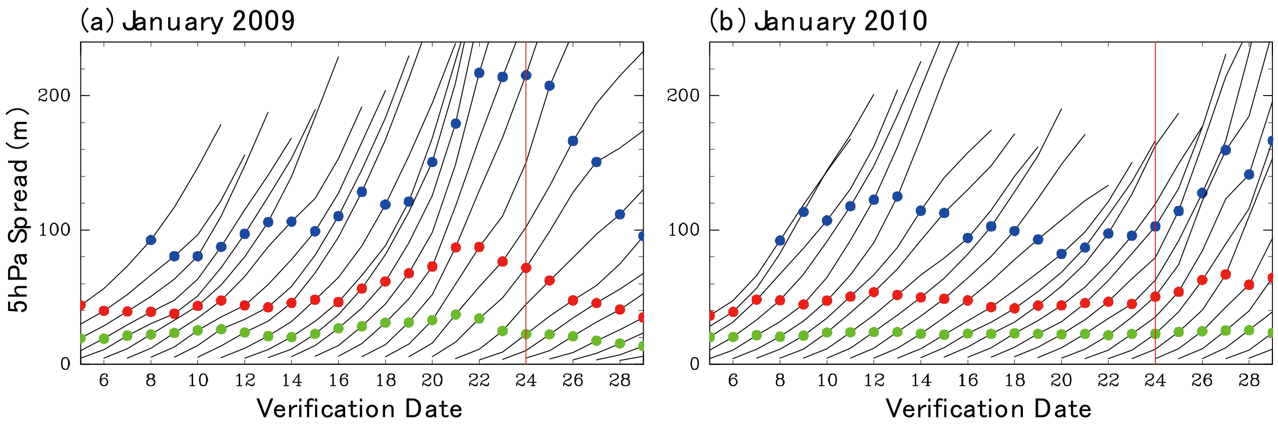

Fig. 4 Time evolution of the rms ensemble spread (m) during the 10-day forecast based on the 5-hPa geopotential height field north of 30°N. See text for the detailed definition of the rms ensemble spread. (a) January 2009, (b) January 2010. Green, red, and blue solid circles indicate 2-day, 4-day, and 7-day forecasts, respectively.

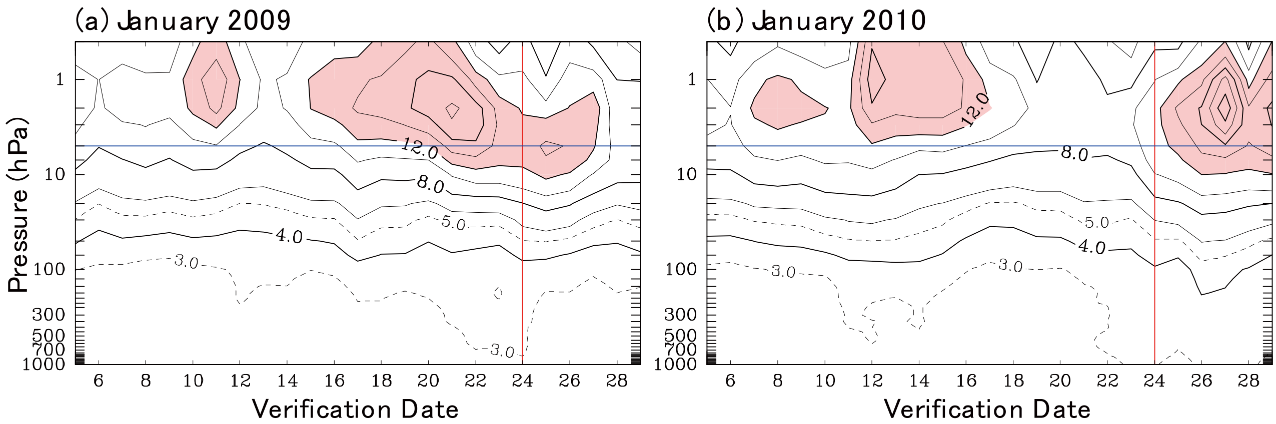

Fig. 5 (a) Amplification rate of the rms ensemble spread during the 4-day forecast at each pressure level (the ordinate) for each verification date (the abscissa) in January 2009. Spreads were evaluated based on geopotential height fields north of 30°N. Regions with an amplification rate larger than 12.0 are shaded red. The red vertical line denotes day 0 (24 January), and the blue horizontal line represents 5 hPa. (b) As in (a), except for January 2010.

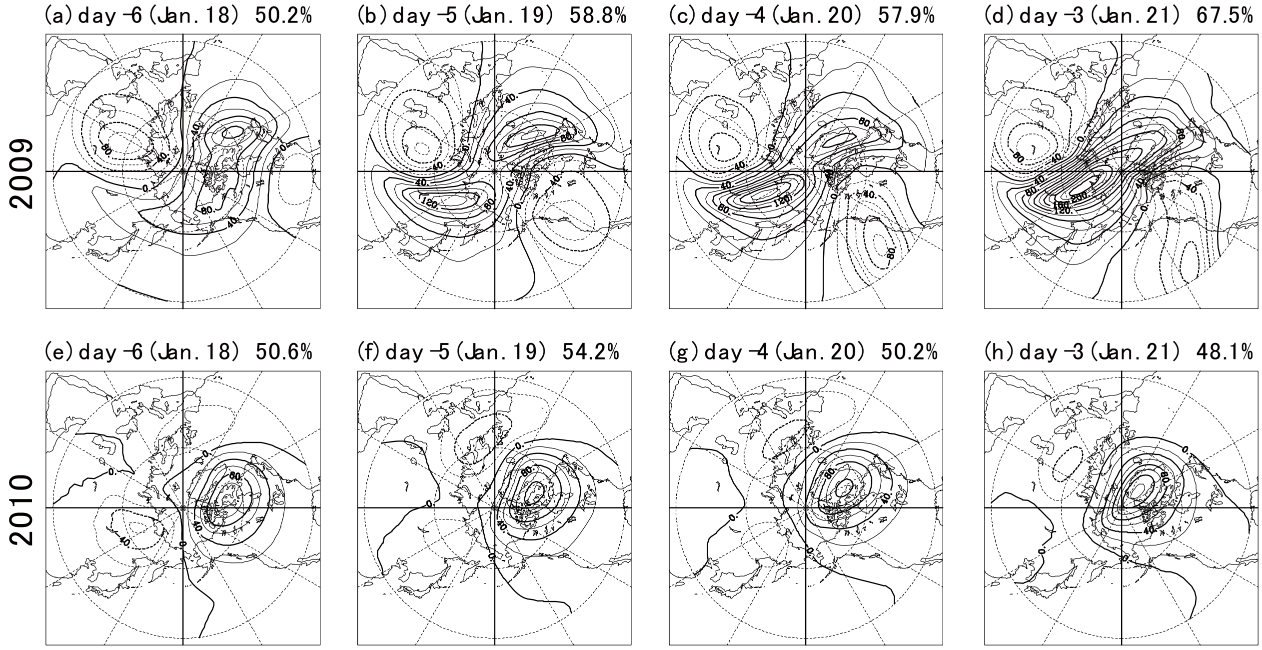

Fig. 6 The 1st EOFs of the difference field of each ensemble member from the ensemble mean prediction of the 5-hPa geopotential height north of 30°N (m) during the onset of the 2009 SSW (top panels) and 2010 SSW (bottom panels) on day −6 (a, e), day −5 (b, f), day −4 (c, g), and day −3 (d, h), computed using 4-day forecasts. Contours are scaled to represent anomalies in meters when the PC is equal to one standard deviation; contour interval is 20 m. Percentage variances associated with the 1st EOFs are shown in the upper right of each panel.

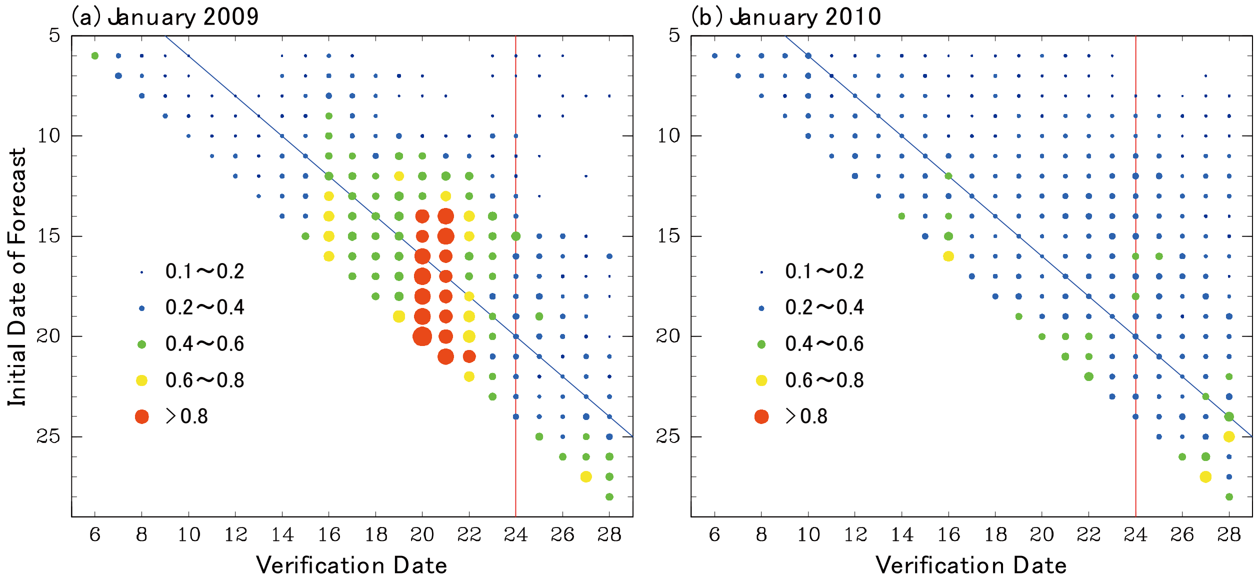

Fig. 7 (a) Growth rate (day^{-1}) of the most unstable mode computed for the basic flow consisting of the T21 truncated 5-hPa stream function of the ensemble mean field on each prediction date (the abscissa) of the forecast starting from 6 to 28 January (the ordinate). The radius of the filled circle is proportional to the growth rate, and its color also indicates the range of the growth rate as shown in the legend. The red vertical line represents day 0 (24 January), and the blue slanting line indicates 4-day forecasts. (b) As in (a), except for January 2010.

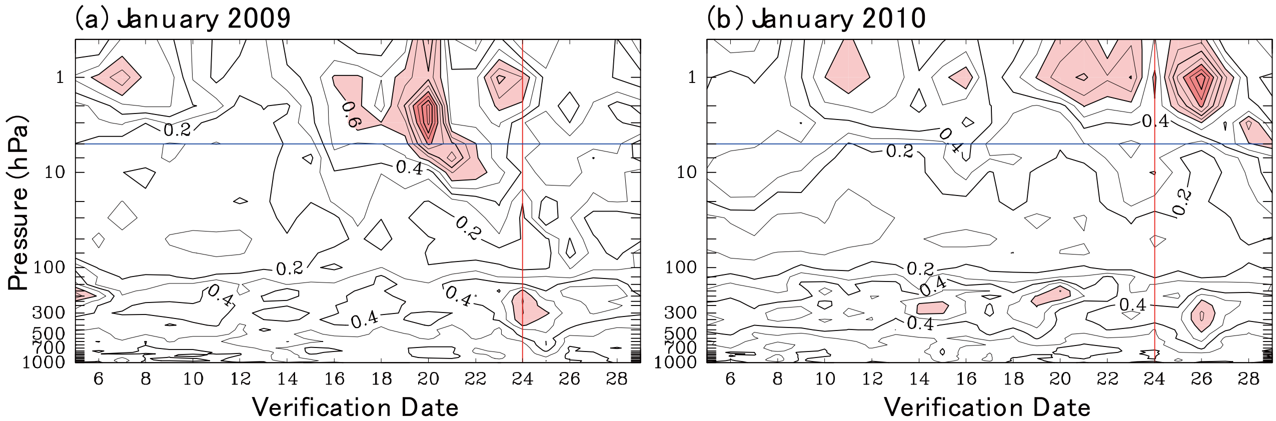

Fig. 8 As in Fig. 5, except for the growth rate (day^{-1}) of the most unstable mode computed for the basic flow consisting of the T21 truncated stream function at each pressure level (the ordinate) of the 4-day ensemble mean forecast. Contour interval is 0.1 day^{-1}, and regions where the growth rate is larger than 0.6 (1.0) day^{-1} are lightly (heavily) shaded in red. (b) As in (a), except for January 2010.

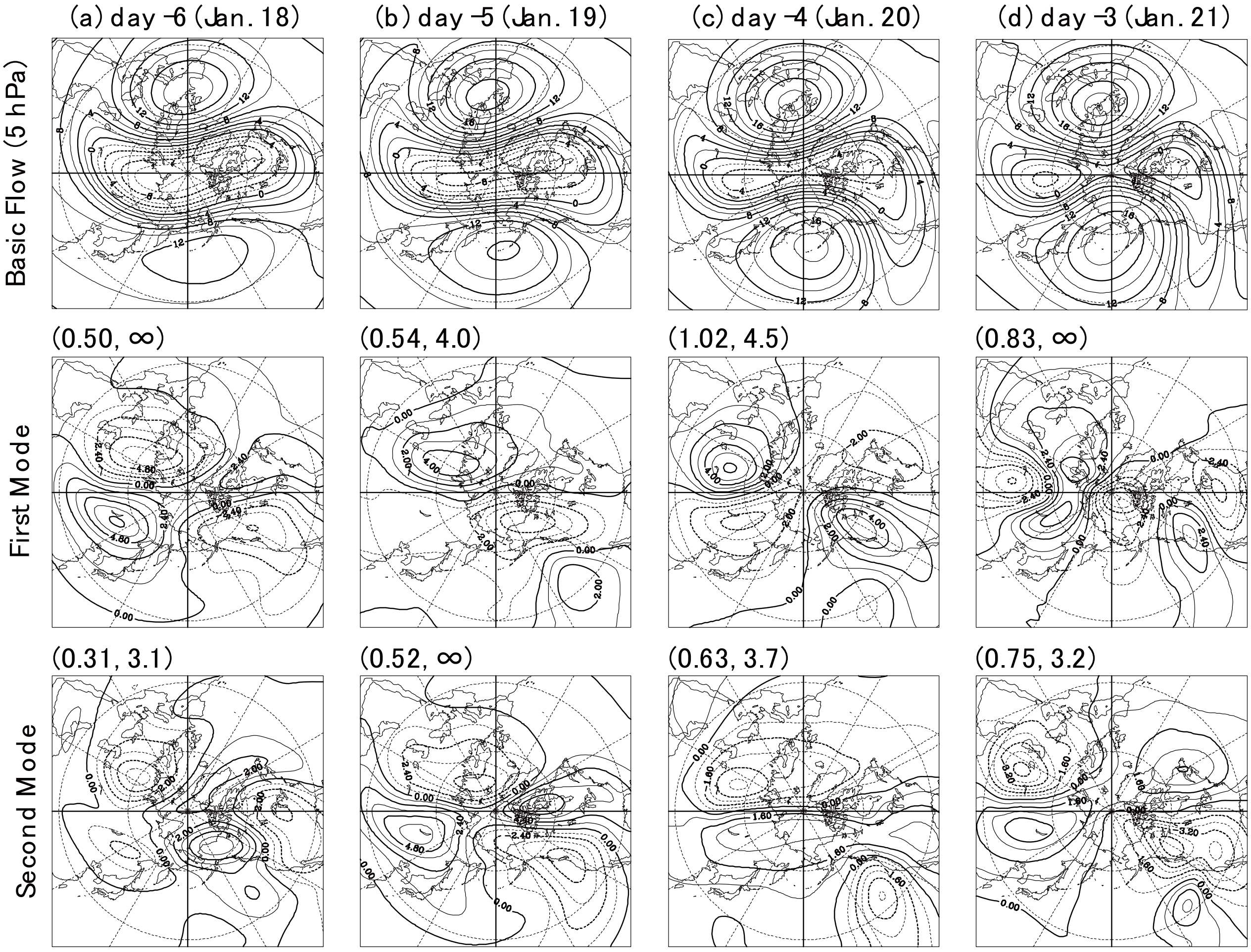

Fig. 9 (top) Horizontal structure of the basic flow given by the T21 truncated 5-hPa stream function field (10^7 m^2 s^{-1}) of the ensemble mean prediction on day −6 (a), day −5 (b), day −4 (c), and day −3 (d) for the 4-day forecasts during January 2009. (middle and bottom) Stream function fields for the first and second unstable modes computed for the basic flow. The first and second numbers in parentheses at the top of each panel indicate the growth rate (day^{-1}) and the period (day) of the unstable mode, respectively. Stationary modes with zero imaginary component of eigenvalues are designated by the period of infinity (∞).

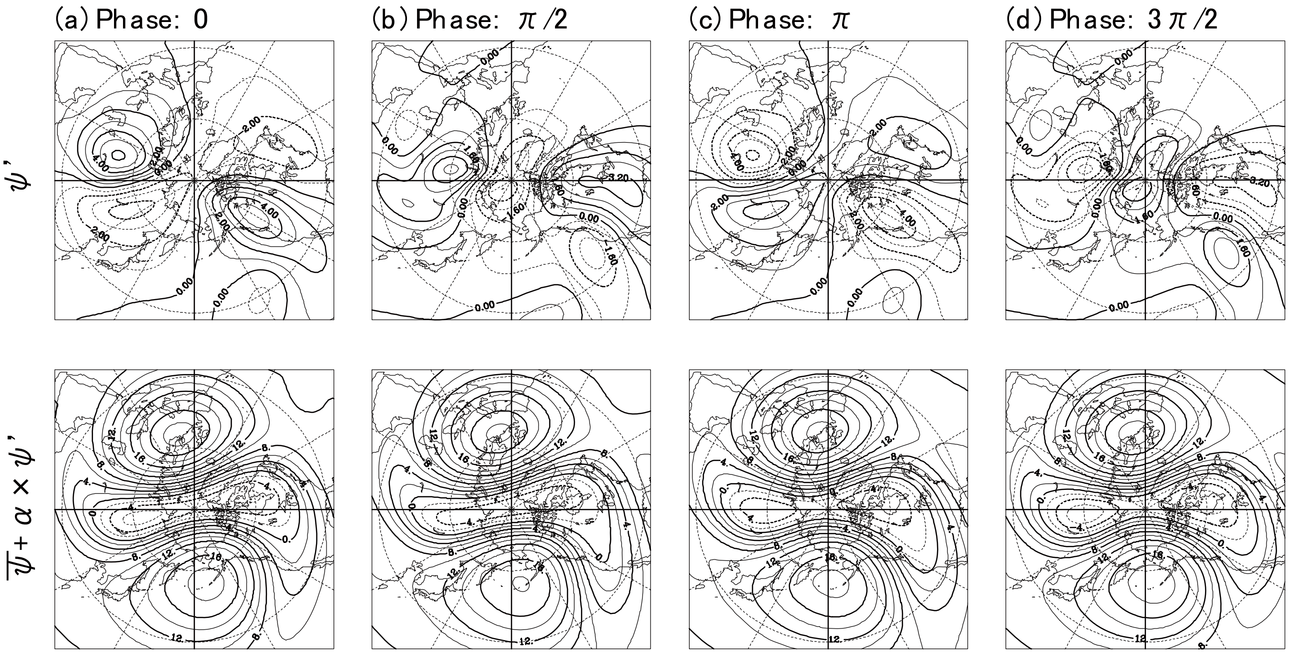

Fig. 10 (top) The stream function field of the most unstable mode (middle panel of Fig. 9c) on day −4 at each 1/4 phase of period 2π: (a) phase 0 (initial), (b) phase $\pi/2$, (c) phase π, (d) phase $3\pi/2$. (bottom) As in top panels, except for the composited stream function field (10^7 m^2 s^{-1}) of the basic flow (top panel of Fig. 9c) and the most unstable mode at each 1/4 phase with amplitude α. The amplitude α is specified so that the square root of the variance of the stream function of the unstable mode at the initial phase (a) is 7.24% of that of the basic flow. The variance is evaluated in the region north of 30°N.

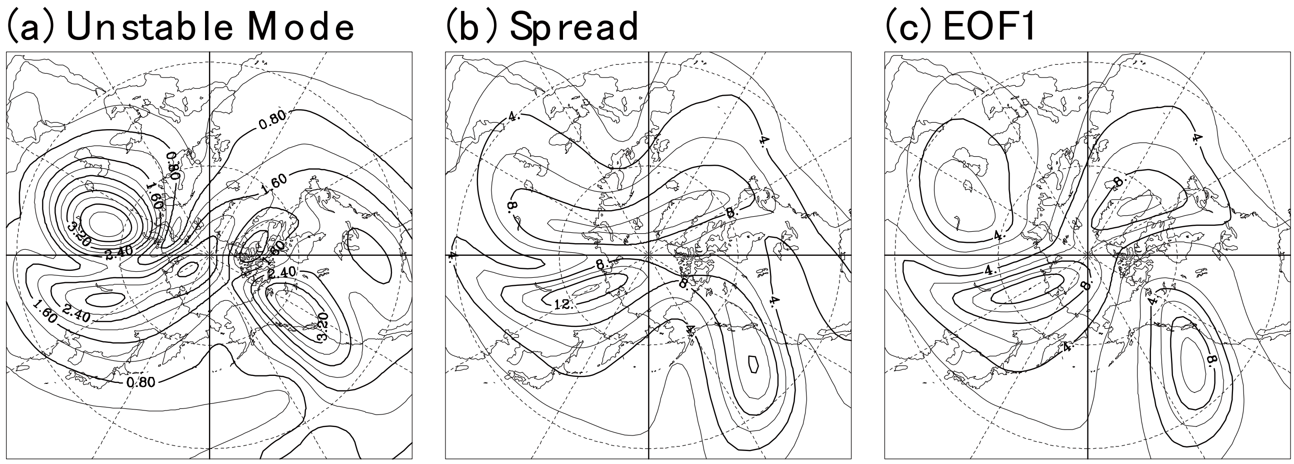

Fig. A1 (a) Horizontal distribution for the square root of the variance of the stream function associated with the phase variation of the most unstable mode on day −4 (middle panel of Fig. 9c). (b) As in (a), except for the square root of ensemble spread of the predicted stream function on day −4, computed using the 4-day ensemble forecast starting from day −7. (c) As in (b), except for the absolute value of the regressed stream function anomaly onto PC1 of the ensemble spread on day −4. PC1 is the corresponding principal component score to the 1st EOF shown in Fig. 6c. Contour interval is 2×10^6 $m^2 s^{-1}$ in (b) and (c). The magnitude in (a) is arbitrary.